Latitudinal Variation in the Color of the Lunar Maria and Implications for Space Weathering

Doug Hemingway[1,2] (djheming@berkeley.edu), Ian Garrick-Bethell[1], Misha Kreslavsky[1]

[1]Department of Earth & Planetary Sciences, University of California Santa Cruz
[2]Now at Miller Institute for Basic Research in Science, University of California Berkeley

- *The color of the Moon varies systematically with latitude*
- *Latitudinal color trend matches the signature observed at lunar swirls*
- *Reduced solar wind flux could account for both color variations*
- *Helps distinguish between effects of solar wind and micrometeoroids*

❶ Introduction and Summary

Space weathering alters the optical properties of exposed surfaces over time, complicating the interpretation of spectroscopic observations of airless bodies like asteroids, Mercury, and the Moon. **Solar wind and micrometeoroids** are thought to be the dominant agents of space weathering, causing exposed surfaces to darken and redden with time, and weakening spectral absorption features, but the **relative contributions of these agents are not yet well understood**.

Using both Clementine and LOLA reflectance data, we report a previously unrecognized systematic latitudinal variation in the near-infrared spectral properties of the lunar maria [1]. We argue that this color trend, which matches the color signature observed at lunar swirls, is the result of reduced solar wind flux at high latitudes. This result could have **implications for the interpretation of spectral observations** from different latitudes and could help to **distinguish between the effects of solar wind and micrometeoroid bombardment** [2-6].

❷ Color Signature of Lunar Swirls

Lunar swirls are optical anomalies that accompany many of the Moon's **crustal magnetic anomalies** [7]. Swirls are bright, superficially resembling immature surfaces such as young impact craters [8-9]. However, **swirls exhibit spectral characteristics that are distinct from those associated with impacts** [10] (Fig. 1). We quantify the two distinct color trends with parameters α and β, defined below (Fig. 2) [1].
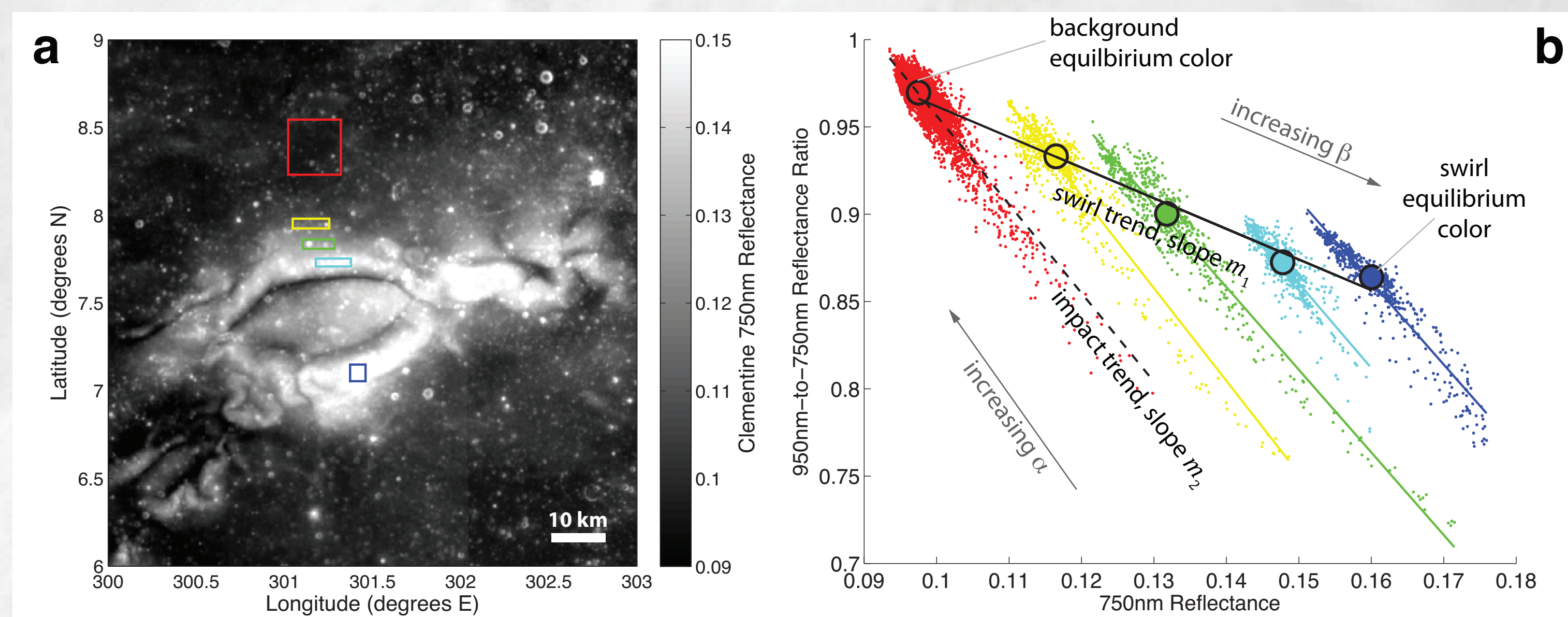

Figure 1: (**a**) 750 nm reflectance at the Reiner Gamma swirl. (**b**) Spectral characteristics (750 nm reflectance versus 950 nm/750nm reflectance ratio) of pixels sampled from the five colored boxes in (**a**). The red point cloud represents a background region whereas the dark blue point cloud corresponds to the brightest part of the swirl. Each of the point clouds displays a steep trend that follows the progression from fresh impact craters (lower right part of each point cloud) to darker background soils (upper left part of each point cloud) [10]; the dashed black line is a best fit through the red point cloud and has a slope of $m_2 = -5.7 \pm 0.5$. The black circles represent the steady state (equilibrium) colors reached with maximum optical maturity in each rectangle. The solid black line is a best fit through the medians (black circles) of each cluster and has a slope of $m_1 = -1.6 \pm 0.2$. Reported slopes are averaged over three separate mare swirl areas [1], and are used to obtain the constants in the equations below.

$$\alpha = R_{750} + 0.625 \left(\frac{R_{950}}{R_{750}} \right) \qquad \beta = R_{750} + 0.175 \left(\frac{R_{950}}{R_{750}} \right)$$
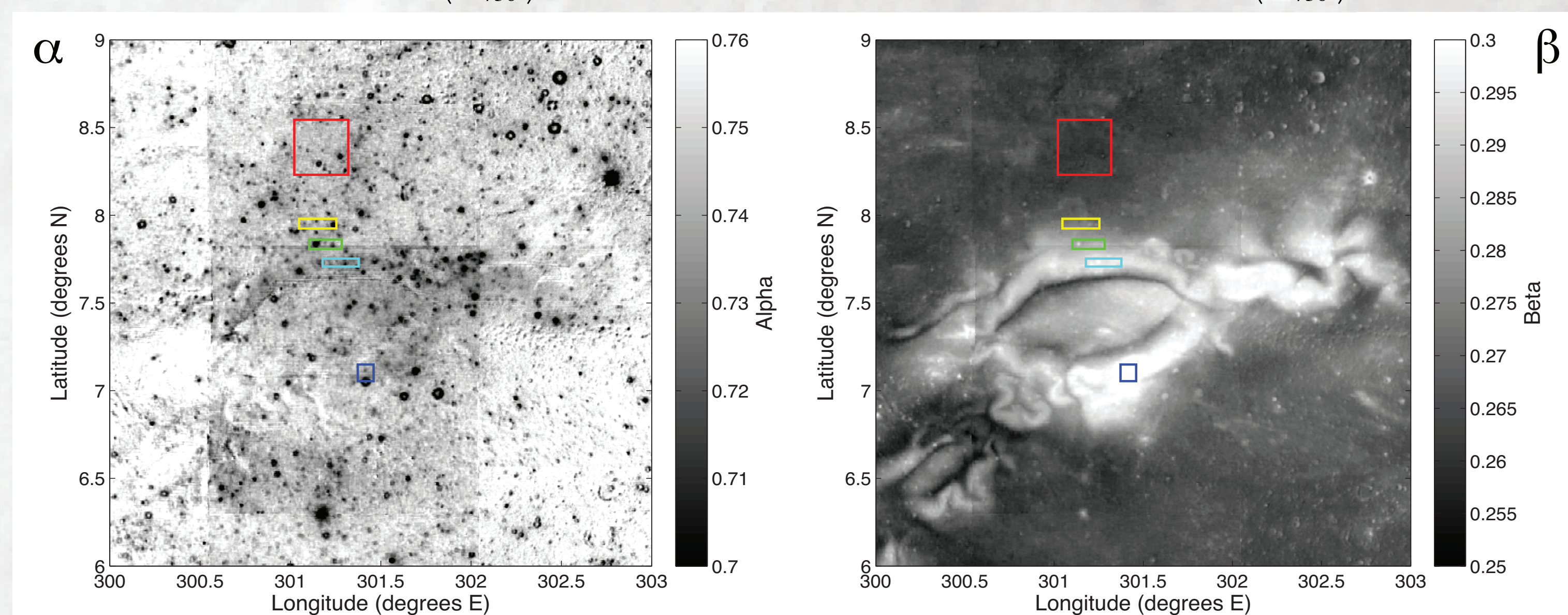

Figure 2: Maps of the α and β parameters (defined above) derived from the swirl- and impact-related trend slopes shown in Fig. 1b. Maps of α show impact craters but not swirl features, whereas maps of β highlight swirl features while impact craters appear muted.

❸ Latitudinal Color Variation

The color of the surface is mainly controlled by mineralogy—this is most obvious in the contrast between the bright, anorthositic highlands and the dark, basaltic maria. The global latitudinal color variation we report here is therefore **not apparent until compositional differences are taken into account**. Once a specific composition is isolated (e.g., Fig. 3a), it becomes clear that equatorial regions are darker and higher in the 950 nm/750 nm band ratio than high latitude regions of the same composition [1].

Similar trends occur over a range of distinct compositions and are especially consistent across the lunar maria (Fig. 3b). In addition to controlling for composition, we verified that the latitudinal color trends we observe are not artifacts of phase angle biases in the Clementine data (Fig. 4), nor can they be explained by contamination from highlands material [1].

The latitudinal color variation is unlike the color trends associated with impacts but **statistically equivalent to those associated with swirls** (Fig. 3b), **suggesting a common mechanism**. Solar wind flux is a good candidate because it is reduced both with increasing latitude (due to increasing incidence angle) and at swirls, where strong magnetic fields may be partially shielding the surface from the impinging solar wind [11-13] (Fig. 5). In contrast, micrometeoroid flux is reduced at high latitudes, but not at magnetic anomalies [14].
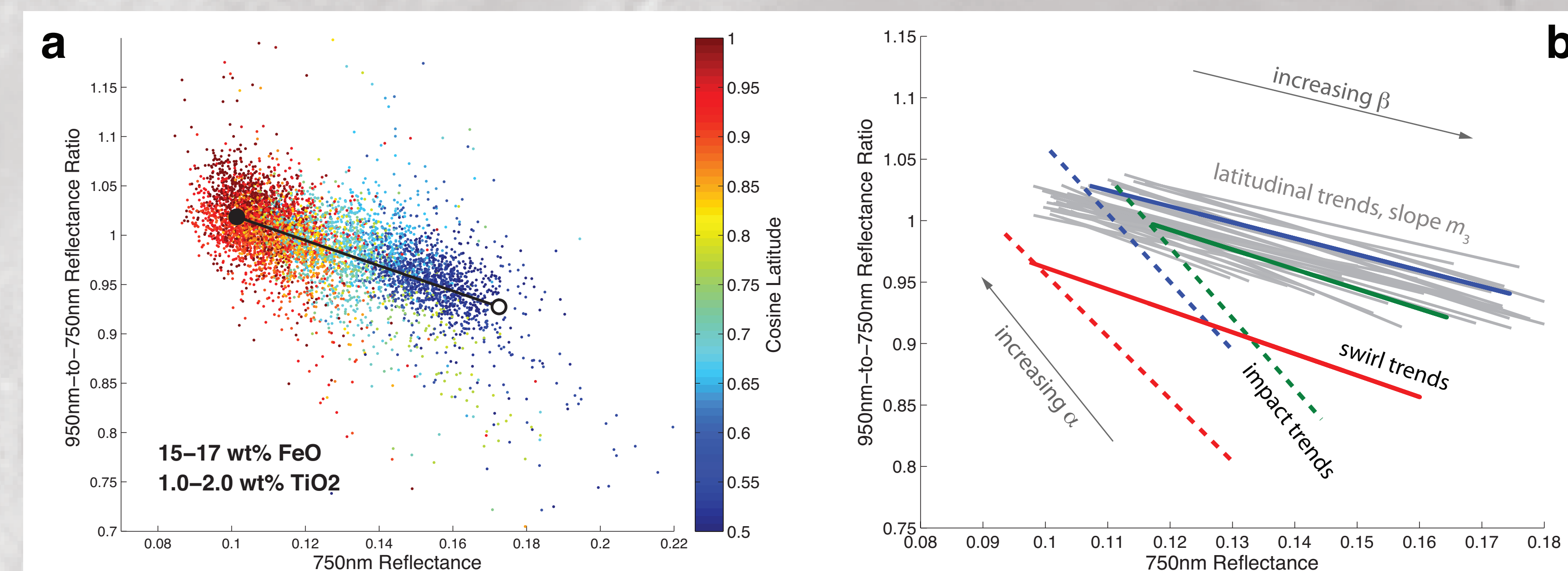

Figure 3: Color variation as a function of latitude. (**a**) Spectral characteristics of pixels sampled from regions with between 15 and 17 wt% FeO and between 1 and 2 wt% TiO_2 [15,16]. Points are color-coded by cosine latitude, illustrating that the optical characteristics of the surface vary systematically with latitude. Equatorial regions (red points) tend to have lower albedo and higher 950 nm/750 nm reflectance ratios than regions farther from the equator (blue points). The black trend line represents a least squares best fit through the data points. The solid black circle corresponds to the color predicted by the best-fit line at the equator and the white circle represents the color predicted at latitudes of ±70°. (**b**) Compilation of the 28 latitudinal trends we examined across the maria (gray lines), one for each compositional bin, compared with the trends found at swirls: the solid red, green and blue lines represent the swirl-related color trends observed at Reiner Gamma, Ingenii, and Marginis, respectively; the dashed lines represent the impact-related color trends observed at each of those swirls. The latitudinal trends have a best-fit slope of $m_1 = -1.5 \pm 0.3$, statistically indistinguishable from the swirl-related trend slope of $m_1 = -1.6 \pm 0.2$.
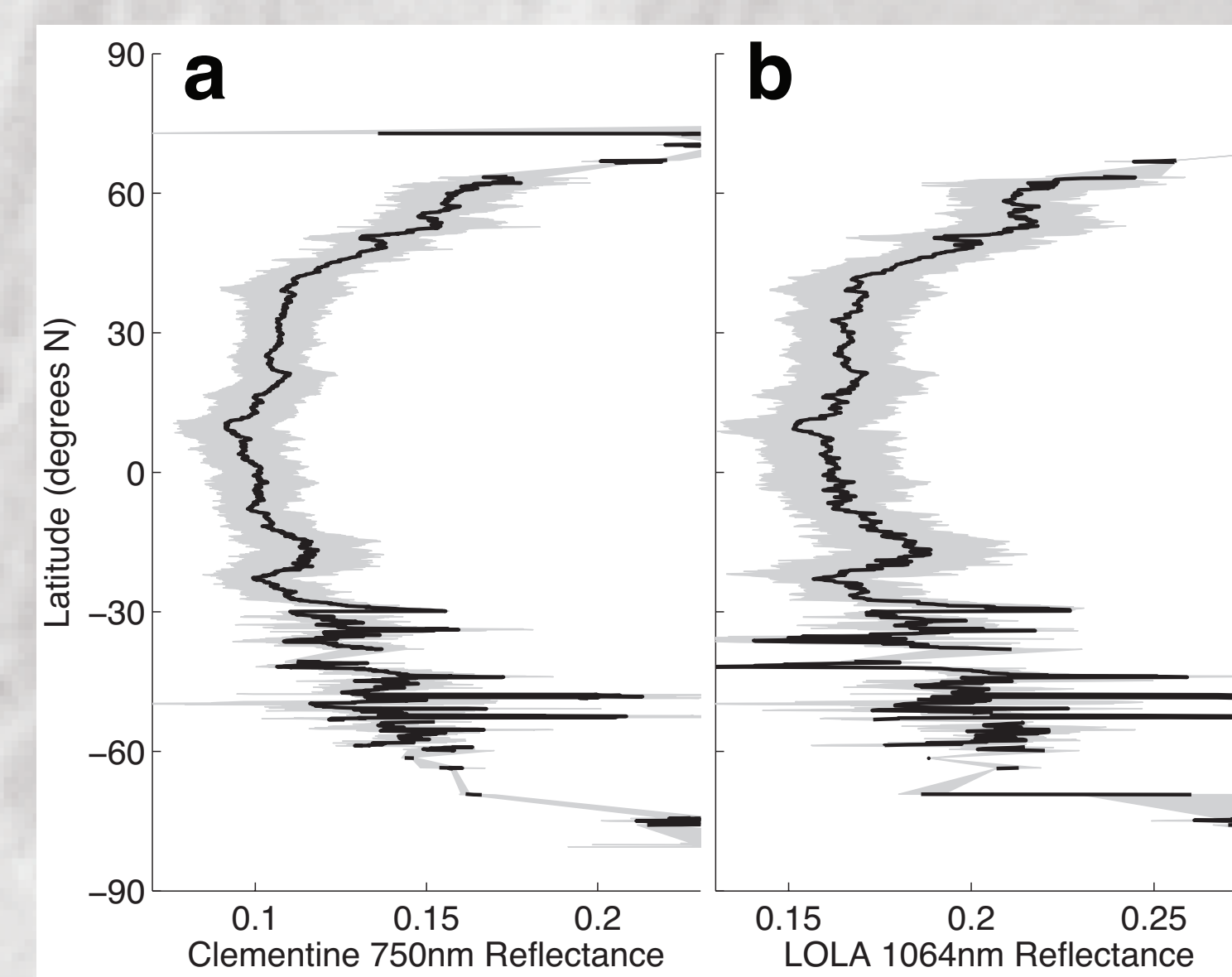

Figure 4: Profiles of (**a**) Clementine 750 nm reflectance [17,18] and (**b**) LOLA 1064 nm reflectance [19] across the lunar maria (as identified according to surface roughness [1,20]). Reflectance tends to be lowest near the equator and higher toward higher northern and southern latitudes, with the curve being approximately symmetric about the equator. The black line and gray band represent the mean and standard deviation at each latitude.
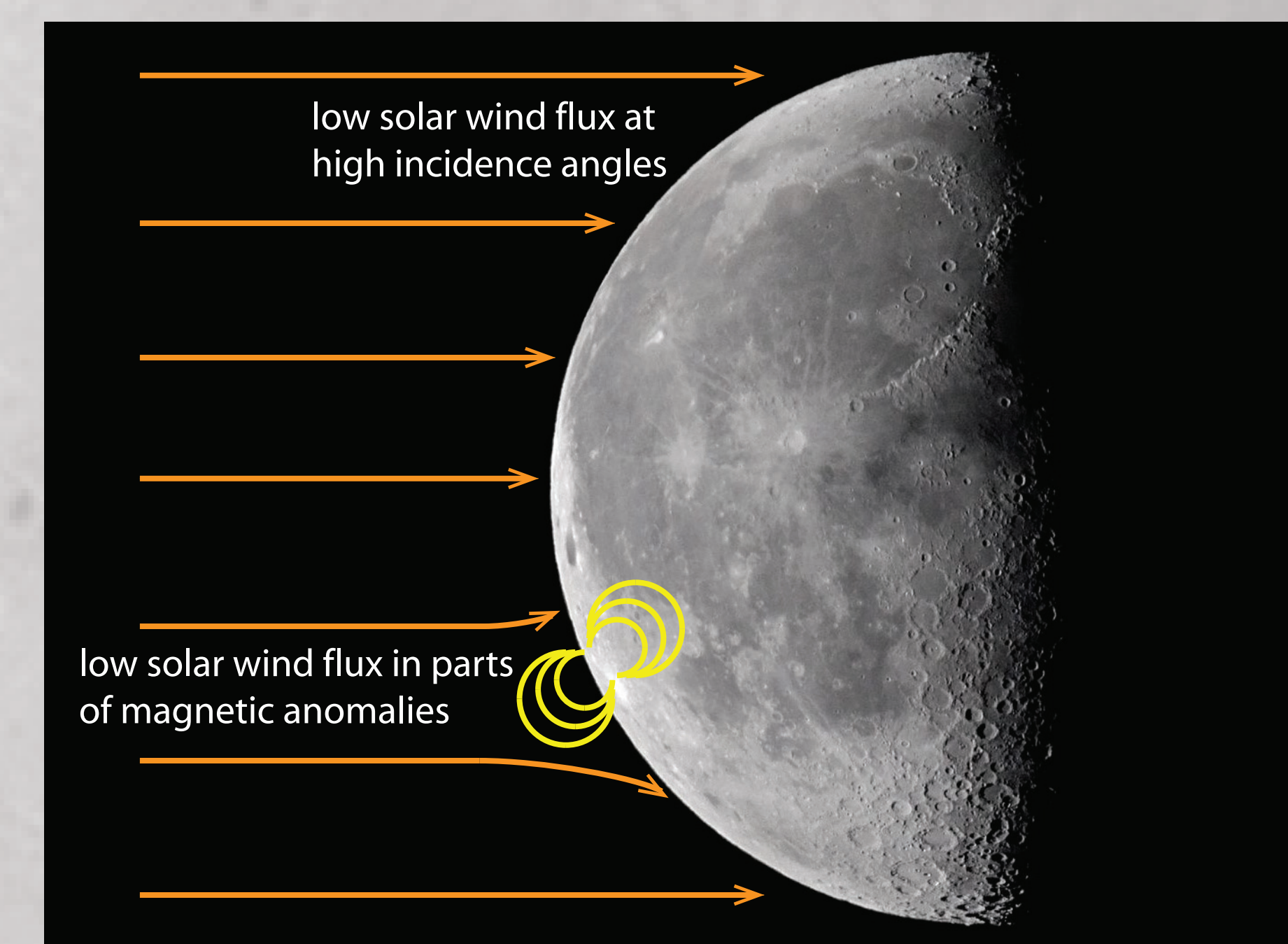

Figure 5: Since the Moon's equator is nearly aligned with the ecliptic plane, the maximum surface flux of solar wind occurs at the equator. At higher latitudes, where the incidence angle is greater, solar wind flux is reduced. Likewise, solar wind flux is very likely reduced at strong magnetic anomalies, due to magnetic deflection of the incoming charged particles and the associated changes in electrostatic potential [12,13,21].

❹ What is this telling us?

Solar wind saturation takes place so rapidly that, even with a 90% reduction in flux, the surface becomes saturated in just ~1 Myrs [4]. This suggests that β is controlled not by total accumulation of solar wind ions, but instead by some **flux-dependent equilibrium**—e.g., between **regolith gardening** and solar wind-induced alteration of exposed grain surfaces.

Over length scales of a few kilometers, the surface exhibits considerable variability in α, whereas variability in β is low (Fig. 1b). This suggests that the **equilibrium β is reached so rapidly** that we do not observe variability in its value over short distances (except perhaps at very young craters), whereas the **evolution of α occurs gradually**, as impact craters transition into mature soils over longer timescales (Fig. 6).
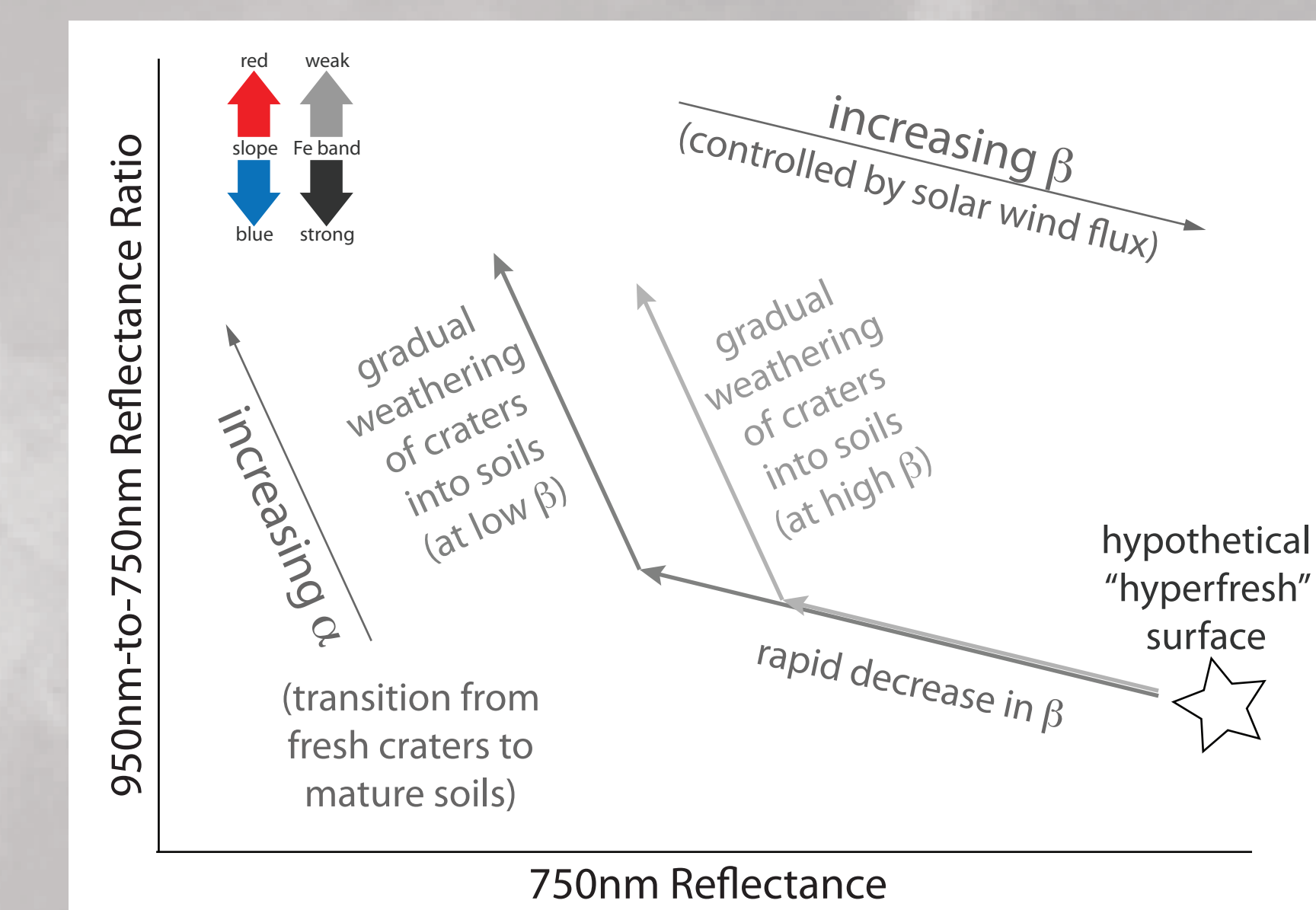

Figure 6: Inferred optical evolution process. For a given composition, all impact craters large enough to excavate fresh material should begin with the same characteristic color (the hypothetical "hyperfresh" point at right). In this model, following the impact event, the freshly exposed material experiences rapid weathering until it reaches an equilibrium value of β, controlled by solar wind flux. This rapid color change occurs primarily in albedo, but is accompanied by a small change in the 950 nm/750 nm band ratio. The crater material then continues to mature gradually (increases in α) until it reaches the local saturation color of the surrounding, well-developed soils. This gradual maturation involves additional darkening, but is also accompanied by a proportionally greater band ratio increase than during the initial mode of rapid weathering.

Based on these observations, and on comparisons with M^3 results [22], we propose that **solar wind weathering takes place relatively rapidly** and involves significant **darkening and reddening**, due perhaps to the accumulation of nanophase iron [4,23]. The gradual transition from bright craters to darker background soils, on the other hand, mainly involves the **weakening of spectral absorption features** along with some additional darkening (Fig. 6). Since it involves no further change in the solar wind-flux dependent β, the latter progression (increasing α) may be driven mainly by **impact vitrification** [24] and the soil's disintegration into increasingly finer grains [25].

References

[1] Hemingway, D. J., Garrick-Bethell, I. & Kreslavsky, M. A. Icarus 261, 66–79 (2015). [2] Pieters, C. M. et al. Meteorit. Planet. Sci. 35, 1101–1107 (2000). [3] Pieters, C. M. et al. Nature 491, 79–82 (2012). [4] Hapke, B. J. Geophys. Res. 106, 10,039–10,073 (2001). [5] Vernazza, P., Binzel, R. P., Rossi, A., Fulchignoni, M. & Birlan, M. Nature 458, 993–5 (2009). [6] Domingue, D. L. et al. Space Sci. Rev. 181, 121–214 (2014). [7] Blewett, D. T. et al. J. Geophys. Res. 116, (2011). [8] Lucey, P. G., Blewett, D. T., Taylor, G. J. & Hawke, B. R. J. Geophys. Res. 105, 20377–20386 (2000). [9] Wilcox, B. B., Lucey, P. G. & Gillis, J. J. J. Geophys. Res. 110, (2005). [10] Garrick-Bethell, I., Head, J. W. & Pieters, C. M. Icarus 212, 480–492 (2011). [11] Hood, L. L. & Schubert, G. Science 208, 49–51 (1980). [12] Hood, L. L. & Williams, C. R. Lunar Planet. Sci. Conf. Proc. 19, 99–113 (1989). [13] Hemingway, D. & Garrick-Bethell, I. J. Geophys. Res. 117, (2012). [14] Richmond, N. C. et al. Geophys. Res. Lett. 30, 1395 (2003). [15] Lawrence, D. J. et al. J. Geophys. Res. 107, 5130 (2002). [16] Prettyman, T. H. et al. J. Geophys. Res. 111, (2006). [17] Nozette, S. et al. Science 266, 1835–1839 (1994). [18] Eliason, E. et al. The Clementine UVVIS Global Lunar Mosaic. (1999). [19] Lucey, P. G. et al. J. Geophys. Res. Planets 119, 1665–1679 (2014). [20] Kreslavsky, M. A. et al. Icarus 226, 52–66 (2013). [21] Poppe, A. R., Fatemi, S., Garrick-Bethell, I., Hemingway, D. & Holmström, M. Icarus (2016, in press). [22] Pieters, C. M., Moriarty, D. P. & Ian Garrick-Bethell. 45th Lunar Planet. Sci. Conf. (2014). [23] Noble, S. K., Pieters, C. M. & Keller, L. P. Icarus 192, 629–642 (2007). [24] Adams, J. B. & McCord, T. B. Science 171, 567–571 (1971). [25] Pieters, C. M., Fischer, E. M., Rode, O. & Basu, A. J. Geophys. Res. 98, 20817–20824 (1993).